Ferrite@tungstate Ceramic Composite as an Efficient Non-Noble Electrocatalyst for the Oxygen Evolution Reaction in Alkaline Media

Irum Jamil , Faisal Nawaz * , Muqdssa Rashid , V. Geethalakshmi , Hsien-Yi Hsu , Mohammed-Ibrahim Jamesh *

Posted Date: 14 January 2026

doi: 10.20944/preprints202601.1084.v1

Keywords: oxygen evolution reaction (OER); electrocatalyst; ferrite; heterostructure; tungstate; non-noble metal catalyst

 doi:10.20944/preprints202601.1084.v1

Article

Ferrite@tungstate Ceramic Composite as an Efficient Non-Noble Electrocatalyst for the Oxygen Evolution Reaction in Alkaline Media

Irum Jamil [1], Faisal Nawaz [1,*], Muqdssa Rashid [1], V. Geethalakshmi [2], Hsien-Yi Hsu [3,4] and Mohammed-Ibrahim Jamesh [3,4,5,*]

[1] Department of Chemistry, University of Wah, 47040, Quaid Avenue, Rawalpindi, Punjab, Pakistan
[2] Department of Chemistry, KIT - Kalaingar Karunanidhi Institute of Technology, Coimbatore, India
[3] School of Energy and Environment, Department of Materials Science and Engineering, Centre for Functional Photonics (CFP), City University of Hong Kong, Hong Kong 999077, China
[4] Shenzhen Research Institute of City University of Hong Kong, Shenzhen 518057, Guangdong, China
[5] Department of Chemistry, Hindusthan College of Engineering and Technology, Coimbatore-641032, Tamil Nadu, India
* Correspondence: faisal.nawaz@uow.edu.pk (F.N.); jmohammed2-c@my.cityu.edu.hk (M.-I.J)

Abstract

The development of efficient, earth abundant electrocatalysts for the oxygen evolution reaction (OER) is essential for alkaline water electrolysis. In this work, we prepared ferrite, tungstate, and ferrite@tungstate heterostructure by simple co-precipitation and hydrothermal routes and evaluated them as OER catalysts in 1 M KOH. The catalysts are characterized by XRD, UV–Vis, FTIR, SEM, and EDX. The catalysts exhibit phase-pure components with intimate contact between the two phases, and a smaller particle size for the composite. The ferrite@tungstate exhibits modified electronic structure possibly due to the electronic interaction between Fe and W centers. Electrochemical measurements demonstrated an overpotential of 200 mV at 10 mA cm-2, that exhibits a reduced Tafel slope (150 mV dec^{-1}), and displays lower charge-transfer resistance than the single-phase oxides. In addition, the composite retains >94% of its current over 24 h, indicating good durability. These results suggest that ferrite–tungstate coupling can be an effective strategy to non-noble OER catalysts.

Keywords: oxygen evolution reaction (OER); electrocatalyst; ferrite; heterostructure; tungstate; non-noble metal catalyst

1. Introduction

The elevation of energy demand and decrease of fossil fuels including petroleum, coal, and natural gas are essential challenging issues that lead to designing of efficient energy storage devices and discovering of earth abundant alternative energies including batteries, perovskite solar cells, and photocatalytic/electrocatalytic generation of hydrogen [1–19]. Water electrolysis is one of the most direct routes to green hydrogen but its efficiency is strongly limited by the oxygen evolution reaction (OER). OER is characterized by much slower intrinsic kinetics than hydrogen evolution reaction (HER), requiring a substantially higher overpotential to overcome the energy barriers of its multiple proton-coupled electron transfer steps with the formation of high energy oxygenated intermediates on the catalytic surface. These limitations lead to high overpotential and accelerate electrode degradation, thereby limiting long-term operational efficiency [20]. Oxide-based catalysts containing Ir and Ru achieve high OER activity and typically reach 10 mA cm^{-2} at relatively low overpotentials of 280 to 320 mV. However, their limited availability, high cost, and instability under prolonged alkaline operation restrict their feasibility for large-scale deployment [21]. This motivates the

 doi:10.20944/preprints202601.1084.v1

development of earth-abundant, structurally stable, and economically feasible alternatives capable of approaching the activity of noble-metal oxides [22,23].

In this context, transition-metal ferrites have emerged as compelling candidates due to their tunable cation distributions, strong metal–oxygen frameworks, and chemical durability under alkaline conditions [24,25]. Among them, Mn–Zn ferrites ($Mn_xZn_{1-x}Fe_2O_4$) are particularly attractive because the interplay between Mn^{2+}, Zn^{2+}, and Fe^{3+} modulates charge density and promotes Fe-centered redox transitions essential for OER [26]. Multiple studies have reported that Mn–Zn ferrites can achieve overpotential in the 350–450 mV range, making them reasonably active among non-noble catalysts [20,24,27]. Despite these advantages, their performance is often constrained by sluggish charge-transfer kinetics, limited electrical conductivity, and the formation of parasitic secondary iron-oxide phases during cycling. These issues reduce the availability of active sites and hinder long-term operation [28,29].

The rational design and engineering of earth-abundant mixed-metal systems whose electronic environments can mimic or approximate those found in noble-metal oxides is essential for developing low-cost catalysts. The key lies in precisely controlling composition, crystal structure, and interfacial chemistry to enhance activity and stability simultaneously [30]. As such, composite or hetero structured materials provide a pathway for tailoring local electronic environments and achieving synergistic catalytic behavior [31]. In this context, constructing hetero structures with oxides that possess high metal oxygen covalency such as tungstates, offers a promising approach. Strontium tungstate ($SrWO_4$) exhibits strong W–O bonding and chemical stability, and although its intrinsic OER activity is limited by a wide band gap ~3.5 eV, its electronic structure makes it well suited to modify adjacent transition-metal sites [32,33]. By interfacing $SrWO_4$ with Mn–Zn ferrite can facilitate electron transfer across the boundary, redistribute local charge density, tune Fe 3d orbital occupation, and stabilize high-valence Fe–O and Fe=O intermediates that could potentially decrease energy barrier in the rate-determining steps of OER. Such interfacial modulation can lower activation barriers, increase active-site turnover, and enhance resistance to surface oxidation [32,34].

However, ferrite tungstate hybrids especially heterostructure $MnZnFe_2O_4$@$SrWO_4$ remain largely unexplored, and their interfacial electronic interactions have not been systematically evaluated. Filling this gap is essential for understanding how such combinations influence catalytic behavior and how compositional and structural engineering can be leveraged to advance OER catalyst design. Motivated by these considerations, this work reports the synthesis of $MnZnFe_2O_4$, $SrWO_4$, and a $MnZnFe_2O_4$@$SrWO_4$ heterostructure composite, followed by a comprehensive investigation of their structural, optical, and electrochemical properties. The goal is to elucidate how ferrite–tungstate coupling modifies the surface chemistry, charge-transfer characteristics, and overall OER performance. The insights gained from this study highlight the potential of $MnZnFe_2O_4$@$SrWO_4$ as a durable, low-cost catalyst and provide guiding principles for designing next-generation, earth-abundant electrocatalysts

2. Experimental Procedure

2.1. Chemicals Required

All reagents were purchased from Sigma-Aldrich and used as received, including strontium nitrate ($Sr(NO_3)_2$) (99%), sodium tungstate dihydrate ($Na_2WO_4{\cdot}2H_2O$) (99%), potassium hydroxide (KOH) pellets (90%), manganese nitrate tetrahydrate ($Mn(NO_3)_2{\cdot}4H_2O$) (98%), Zinc nitrate hexahydrate ($Zn(NO_3)_2{\cdot}6H_2O$) (≥98%), iron (III) nitrate nonahydrate ($Fe(NO_3)_3{\cdot}9H_2O$) (98%), cetyltrimethylammonium bromide (CTAB, surfactant) (99%) and ethanol (C_2H_5OH) (99.8%). Deionized water (2.0 MΩ/cm) was used.

 doi:10.20944/preprints202601.1084.v1

2.2. Synthesis of Strontium Tungstate ($SrWO_4$)

Strontium tungstate ($SrWO_4$) nanoparticles synthesis was performed using a co-precipitation approach [35]. Initially, two separate 0.40 M solutions were prepared by dissolving 1.27 g of $Sr(NO_3)_2$ and 1.98 g of $Na_2WO_4{\cdot}2H_2O$ in 15 mL of deionized water under moderate stirring at ambient temperature. The strontium solution was then added dropwise into the tungstate solution under vigorous stirring. The reaction mixture was heated to 70 °C and maintained under constant stirring for 3 h, while the pH was adjusted and stabilized at 8.0 using aqueous KOH to ensure controlled nucleation. This leads to the formation of fine white precipitate. After 3 h, the suspension was left to age for 12 h at ambient temperature to allow the growth of the particles. The resulting precipitate was then centrifuged at 5000 rpm and washed repeatedly with deionized water until the supernatant is clear. The resultant solid was dried at 80 °C to eliminate surface moisture, followed by calcination at 200 °C for 2 hrs in a muffle furnace, producing well-crystallized $SrWO_4$ nanoparticles.

2.3. Synthesis of Manganese Zinc Ferrite ($MnZnFe_2O_4$)

$MnZnFe_2O_4$ nanoparticles were synthesized via a CTAB assisted co-precipitation method. Stoichiometric amounts of metal nitrates i.e 2.5 mmol of $Mn(NO_3)_2$ (0.717 g), 2.5 mmol of $(ZnNO_3)_2.6H_2O$ (0.743 g) and 10.0 mmol of $Fe(NO_3)_3.9H_2O$ (4.040 g), were separately dissolved in deionized water and diluted to 25 mL each. The solutions were combined under vigorous stirring and CTAB (0.1 %) was used as a steric stabilizer. The mixture was heated to 80 °C, and precipitation was induced by dropwise addition of concentrated KOH solution to maintain pH 10–12. The suspension was aged at 80 °C for 3 h to promote crystallite growth. The product was isolated by centrifugation, washed repeatedly with deionized water and ethanol until neutral pH was achieved, and dried at 80 °C for 12 h. Finally, the powder was calcined at 200 °C for 2 h (5 °C/min ramp) to decompose organics and enhance crystallinity, yielding phase-pure $MnZnFe_2O_4$ nanoparticles.

2.4. Synthesis of $MnZnFe_2O_4$@$SrWO_4$

Heterostructure of $MnZnFe_2O_4$@$SrWO_4$ was synthesized [32]. $MnZnFe_2O_4$ seeds (0.50 g) were dispersed in DI water (30 mL) containing PVP (1 wt%) and sonicated (50 °C, 15 min) as illustrated in Figure 1. Separate 0.10 M solutions of $Sr(NO_3)_2$ (15 mL) and $Na_2WO_4{\cdot}2H_2O$ (15 mL) were adjusted to pH 8.5. Under vigorous stirring (600 rpm) at 80 °C, the Sr^{2+} and WO_4^{2-} solutions were added dropwise over 20 min to the ferrite dispersion while maintaining pH 8 with NH_4OH. The mixture was aged 30 min at 80 °C, transferred to a teflon-lined autoclave, and heated at 140 °C for 6 h. The solid was recovered by centrifugation (8000 rpm, 10 min), washed sequentially with DI water and ethanol to a neutral supernatant, and dried at 80 °C for 2 hours and then calcined in muffle furnace for 200 °C for 2 h.

 doi:10.20944/preprints202601.1084.v1

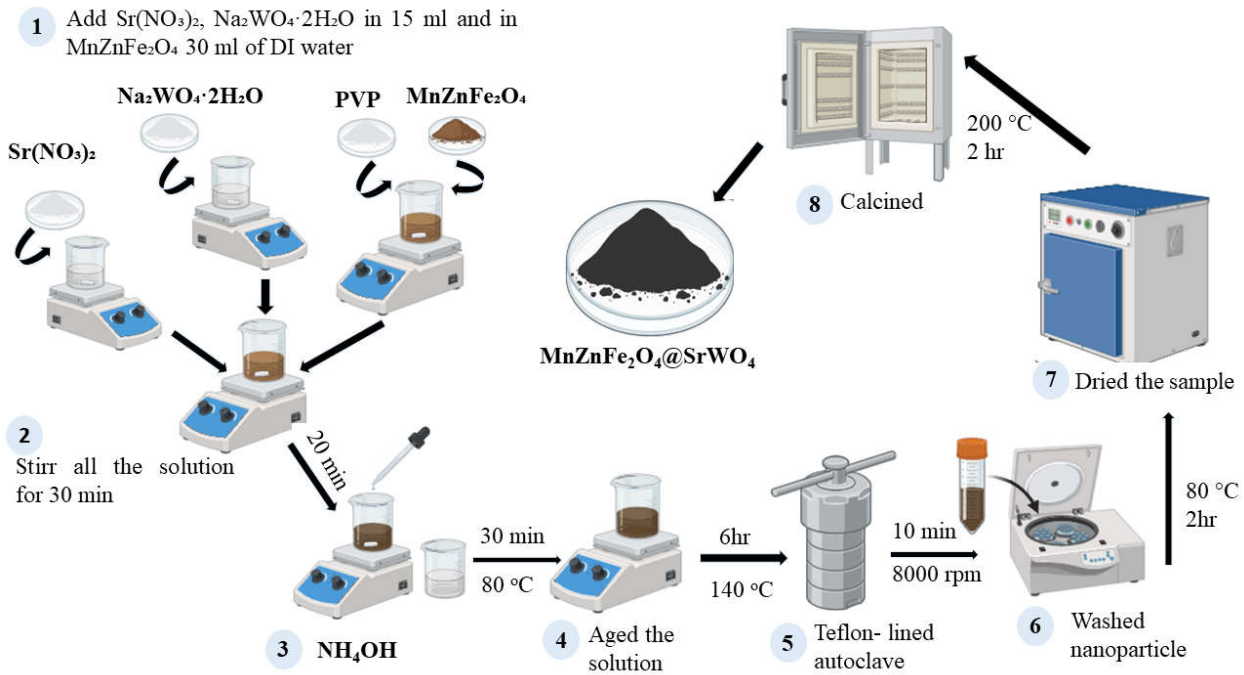

Figure 1. Synthetic scheme for the preparation of $MnZnFe_2O_4$@$SrWO_4$.

2.5. Preparation of Working Electrode for OER

All electrochemical investigations were carried out using a computer controlled electrochemical workstation, potentiostat (PGSTAT 302 N) from Metrohm AUTO LAB in a typical three-electrode setup using an Ag/AgCl electrode as the reference electrode, a Pt electrode as the counter electrode and the prepared $MnZnFe_2O_4$, $SrWO_4$ and $MnZnFe_2O_4$@$SrWO_4$ electrocatalysts as the working electrode. The electrode substrate is glassy carbon electrode. The Ag/AgCl reference electrode was calibrated with respect to reversible hydrogen electrode (RHE) using the following equation 1.

$$E_{RHE} = E_{Ag/AgCl} + (0.059 \times pH) + E^{\circ}_{Ag/AgCl}\ (0.197\ V) \quad (1)$$

All electrochemical tests were carried out in alkaline electrolyte (1 M KOH). To prepare the working electrode, 3 mg of catalyst was taken in a 1.5 mL microcentrifuge tube and dissolved with a mixed solution of 70 µL of deionized water and 110 µL of isopropanol. Afterward, the resulting mixture was subjected to sonication for 30 minutes to ensure primary particle dispersion. Next 30 µL of 5 % Nafion solution was introduced as the polymeric binder. The entire suspension was then thoroughly sonicated for another 60 min to obtain a homogeneous ink. The prepared slurry of catalyst ink was drop coated onto the electrode surface having an area of 0.0314 cm^2 (2 mm) and then it was left for drying in an oven for 30 min. The resulting electrode was used as a working electrode (WE) for the study of oxygen evolution reaction (OER).

2.6. Characterizations

The optical properties of the samples were examined using a double-beam UV–Vis spectrophotometer (AI Specord 200 Plus, Analytik Jena, Germany). The instrument operates over a wavelength range of 190–1100 nm with a 1 nm slit width and a scan rate of 200 nm min^{-1}, and uses both D_2 and W-halogen lamps as light sources. Tauc plots are used to determine the band gap (eV) of $MnZnFe_2O_4$ and tungstate by plotting $(\alpha h\nu)^{1/2}$ versus hν (eV). Structural characterization was carried out with an X'Pert³ MRD diffractometer (Malvern Panalytical, Netherlands) equipped with a Cu Kα radiation source (λ_1 = 1.5406 Å, λ_2 = 1.5444 Å). The measurements were performed at 25 °C with a 2θ scan rate of 1° min^{-1} and minimum step sizes of 0.001° (ω) and 0.1° (φ), using a reflection–transmission spinner stage. Surface morphology was observed using a Sigma 300 field-emission scanning electron microscope (ZEISS, Germany), operated at 0.02–30 kV and capable of

 doi:10.20944/preprints202601.1084.v1

magnifications from 10× to 1,000,000×. FTIR measurements were performed using an Alpha-ATR spectrometer (Bruker, Germany) over the 4000–400 cm^{-1} range with a resolution of 4 cm^{-1}, averaging 32 scans per sample. Elemental composition was analyzed using the Smart EDX system (ZEISS, Germany), integrated with the Sigma 300 SEM, offering an energy resolution of about 129 eV (at 1–5 nA) and supporting magnifications between 5,000× and 50,000× with a Si_3N_4 window for light-element detection.

3. Results and Discussion

3.1. Crystallographic Study

The crystal structure and phase purity of $Mn_{0.5}Zn_{0.5}Fe_2O_4$, $SrWO_4$ and the $SrWO_4$@$MnZnFe_2O_4$ composite were examined by powder XRD (Cu Kα, $\lambda \approx 1.5406$ Å). The diffraction patterns are shown in Figure 2. The diffraction pattern of the $SrWO_4$ powder is completely different and can be indexed to a tetragonal scheelite structure (space group $I4_1/a$). Distinct peaks are observed at 2θ values typical of $SrWO_4$, which we assign to the (101), (112), (004), (200), (211), (204), (220), (116), (312), (224) and (136) planes, in agreement with the scheelite-type earlier reports on nanocrystalline $SrWO_4$ with JCPDS 96-591-0264 (marked in red colored rectangle shape [36]. No additional peaks from SrO, WO_3 or other tungstate phases are detected, confirming that the co-precipitation route followed by mild calcination at 200 °C yields phase-pure $SrWO_4$ with good crystallinity. Similar diffraction behavior has been reported by Fathima et al. [37] and by Chen et al. [38] who also observed a predominant (112) reflection and characteristic (211) peaks for chemically synthesized $SrWO_4$.

The XRD pattern of the $MnZnFe_2O_4$ sample exhibits a series of well-defined peaks at around 2θ of ≈ 30°, 35°, 43°, 53°, 57°, 62° and 74°. These reflections can be indexed to the (220), (311), (400), (422), (511), (440) and (533) planes of a cubic spinel ferrite with space group $Fd\bar{3}m$. The peak positions and their relative intensities agree well with the $Mn_{0.5}Zn_{0.5}Fe_2O_4$ reference pattern (JCPDS 96-230-0585) reported in the literature [24,34]. This confirms that the main phase formed in our synthesis is nanocrystalline $MnZnFe_2O_4$. Besides the spinel peaks, a set of much weaker reflections is also visible in the $MnZnFe_2O_4$ pattern at 2θ of ≈ 24°, 33°, 35.5°, 40.8°, 49.4°, 54.0°, 57.5°, 62.4°, 63.9° and 71.9°. These can be indexed to the (012), (104), (110), (113), (024), (116), (018), (214) and (300) planes of rhombohedral α-Fe_2O_3 (hematite; marked in pink colored oval shape; JCPDS 33-0664) [34]. Their very low intensity compared with the spinel (311) peak indicates that hematite is present only as a minor secondary phase in the as-prepared $MnZnFe_2O_4$ powder, most likely due to partial oxidation of iron during the ferrite synthesis and calcination. $MnZnFe_2O_4$ prepared via sol–gel, co-precipitation, and combustion synthesis has repeatedly exhibited similar XRD signatures in the literature [6,7], confirming the reliability of the structural assignment.

For the $SrWO_4$@$MnZnFe_2O_4$ composite, the XRD pattern looks like a superposition of the two individual patterns. The spinel ferrite peaks corresponding to the (220), (311), (400), (422), (511) and (440) planes are still clearly present (marked in green colored rectangle shape; JCPDS 96-230-0585), showing that the $MnZnFe_2O_4$ phase keeps its cubic structure after composite formation. At the same time, the characteristic scheelite peaks indexed as (112), (004), (200), (204), (220), (116), (312) and (224) of $SrWO_4$ with JCPDS 96-591-0264 (marked in red colored rectangle shape are also visible, confirming that both components coexist in the final material. The 2θ positions of these reflections remain essentially unchanged compared with the pure phases, indicating that there is no formation of a new bulk mixed phase and that the interaction between $MnZnFe_2O_4$ and $SrWO_4$ occurs mainly at the interface. Comparable behavior has been reported for ferrite oxide composites, where the individual crystalline frameworks remain structurally preserved during composite formation [32].

A key point is that, in the composite pattern, the small hematite-related peaks that were visible in the pristine $MnZnFe_2O_4$ sample are no longer observed in composite. In particular, the diagnostic α-Fe_2O_3 reflections near 2θ ≈ 24° and 33° are absent. This disappearance can be attributed to surface encapsulation of the ferrite nanoparticles by the $SrWO_4$ shell, which suppresses the diffraction contribution of any surface-bound hematite, and secondly the reduced Fe oxidation during the

 doi:10.20944/preprints202601.1084.v1

composite's hydrothermal step, where the presence of WO_4^{2-} species offers a stabilizing chemical environment that discourages the formation of Fe–O–Fe clusters associated with hematite. Similar observations have been reported for ferrite–tungstate and ferrite–molybdate composites, where the secondary oxide layer inhibits surface oxidation. [10,11].

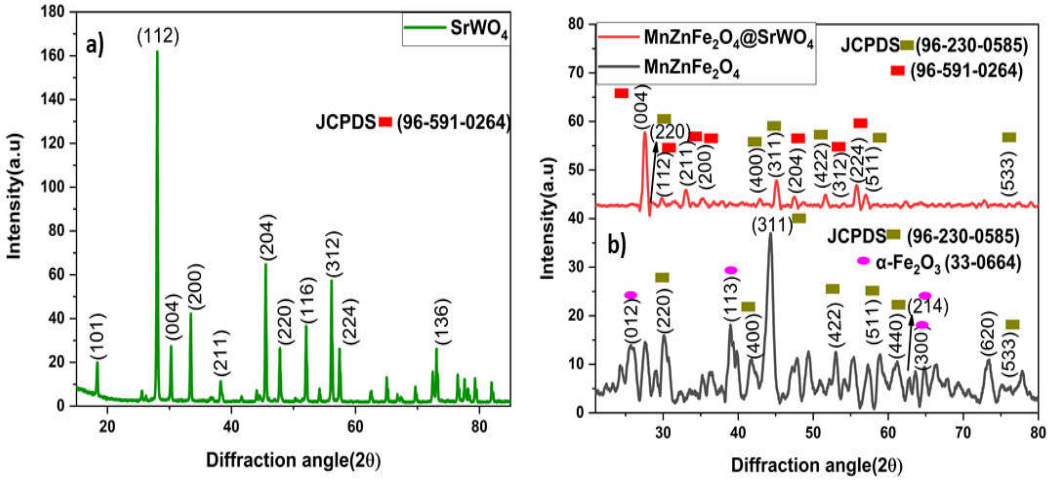

Figure 2. XRD patterns of a) $SrWO_4$ b) $MnZnFe_2O_4$ and $MnZnFe_2O_4$@$SrWO_4$.

The average crystallite sizes were estimated using the Debby Scherer equation.

$$D = \frac{K\lambda}{\beta \cos\theta} \quad (2)$$

where,

K= Scherer constant (0.9)

λ= Wavelength of X-rays used (1.5406 A° for Cu Kα)

β= Full width at half maximum (FWHM) value

θ= Angle of diffraction (2θ)

$SrWO_4$, $MnZnFe_2O_4$, $MnZnFe_2O_4$@$SrWO_4$, exhibit crystalline size of 54.8 nm, 34.3 nm, and 16.8 nm, respectively, which are calculated by using equation (2), while the percent crystallinity of $MnZnFe_2O_4$, $SrWO_4$, and $MnZnFe_2O_4$@$SrWO_4$ is 99.2 %, 96.2 %, and 90 %, respectively. The percent crystallinity was calculated using equation (3). It represents how ordered the atomic arrangement of the material is with respect to the ratio of the crystalline to amorphous phases.

$$\text{Percentage of Crystalinity}(\%) = \frac{\text{Ac}}{\text{Ac}+\text{A}\alpha} \times 100 \quad (3)$$

where,

Ac= area under crystalline peak

Aα= area under the amorphous peak

3.2. Ultra Violet (UV) Spectroscopy

The $MnZnFe_2O_4$@$SrWO_4$ heterostructure exhibits modified electronic structure, which is inferred from the optical absorption behavior and band-gap characteristics of $MnZnFe_2O_4$, $SrWO_4$, and $MnZnFe_2O_4$@$SrWO_4$, while optimal electronic structure is beneficial to enhance the performance for OER. As shown in Figure 3(a–c), $SrWO_4$ has a primary absorption peak at 301 nm, which is attributed to the O 2p → W 5d transitions, that is consistent with its wide band gap of 3.5 eV. While it shows optical activity in the UV region, its large band gap limits its intrinsic electrical conductivity and results in a high charge-transfer resistance (which will be discussed later) under standard electrochemical conditions. This inherent electronic barrier contributes to its sluggish OER kinetics when used as a standalone catalyst.

Besides, $MnZnFe_2O_4$ absorbs strongly in the visible region with bands at 450 and 620 nm, which is ascribed to the O^{2-} → Fe^{3+} charge-transfer transitions. These transitions can contribute to

 doi:10.20944/preprints202601.1084.v1

performance for OER and they can allow rapid movement of electrons between the O ligands and Fe sites and facilitate the easier formation of Fe^{3+}/Fe^{4+} redox pairs, which could be crucial for OER catalysis. This is consistent with its narrow band gap of 1.81 eV. This can facilitate the intrinsic electrical conductivity and result in a relatively less charge-transfer resistance (which will be discussed later) under standard electrochemical conditions. This can lower electronic barrier, which can enhance OER kinetics when used as a standalone catalyst.

On the other hand, the $MnZnFe_2O_4$@$SrWO_4$ heterostructure has a completely different optical response. There is an absorption peak shift from 301 nm in $SrWO_4$ to 266 nm in the composite, and there is an absorption at 450 nm in the composite, which is ascribed to $MnZnFe_2O_4$, that indicates stronger coupling of the heterostructure. Thus, optimal bandgap of 2.4 eV is observed for $MnZnFe_2O_4$@$SrWO_4$ heterostructure, when compared to that of 1.8 eV of $MnZnFe_2O_4$ and 3.5 eV of $SrWO_4$. Thus, the heterostructure exhibits optimal electronic structure, which can afford active sites with optimal adsorption energy for intermediates for OER, while the optimal bandgap of heterostructure affords relatively high intrinsic electrical conductivity, resulting in a relatively less charge-transfer resistance (which will be discussed later) under standard electrochemical conditions. This can lower electronic barrier, which can enhance OER kinetics when used as a standalone catalyst. Moreover, the formation of interfacial Fe 3d–W 5d hybrid states in the composite lowers the energy barrier for electron transfer and stabilizes high-valence Fe and W species. These hybridized states can accelerate the generation of Fe^{4+}/Fe^{5+} intermediates, which are widely recognized as active species in the lattice-oxygen–mediated mechanism during OER. Additionally, localized defect states arising from slight structural disorder at the heterostructure boundary creates multiple energetically accessible pathways for charge transport, improving catalytic kinetics.

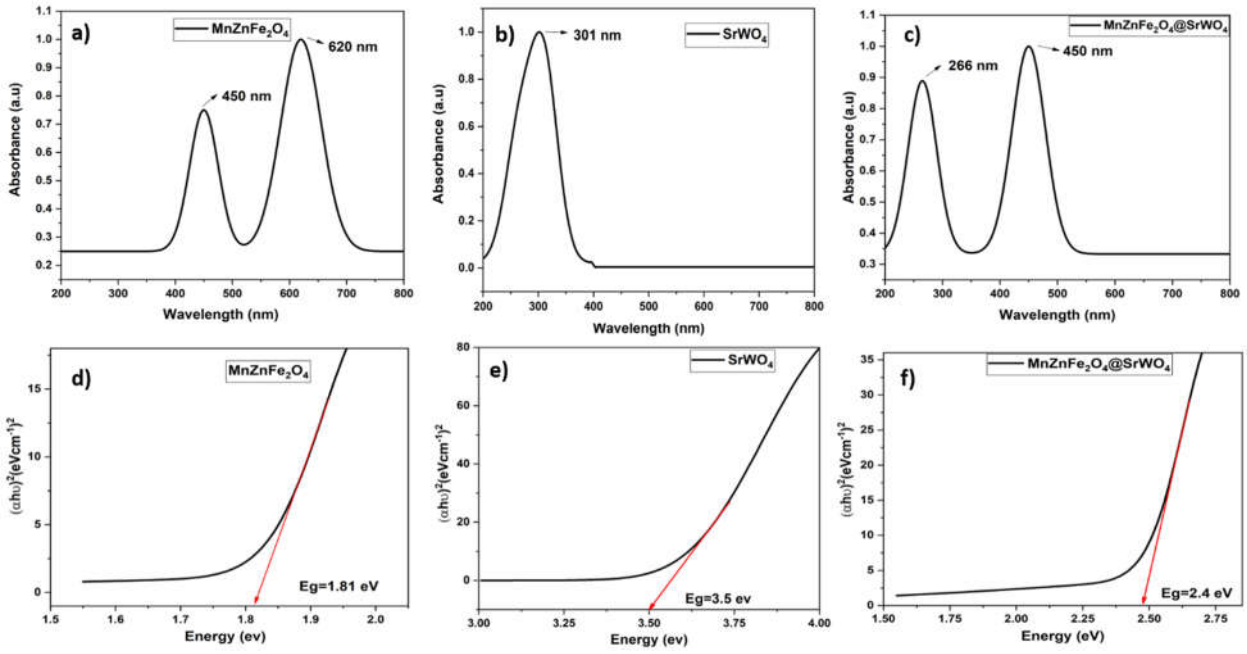

Figure 3. (a–c) UV–Vis spectra and (d–f) Tauc plots of $MnZnFe_2O_4$, $SrWO_4$, and $MnZnFe_2O_4$@$SrWO_4$.

3.3. Fourier Transform Infrared (FTIR) Spectroscopy

The FTIR spectra in Figure 4 clearly reflect the vibrational features of both the $MnZnFe_2O_4$ and $SrWO_4$ phases. For the ferrite sample, two characteristic absorption bands are observed in the lower frequency region. The strong band at about 594 cm^{-1} is attributed to the stretching vibration of metal–oxygen bonds at the tetrahedral sites, while the band near 431 cm^{-1} is ascribed to the octahedral site vibrations of the spinel lattice. These two features are typical of Mn–Zn spinel ferrites and are consistent with earlier reports [39]. A pronounced absorption peak at 835 cm^{-1} is ascribed to the

 doi:10.20944/preprints202601.1084.v1

$SrWO_4$ phase, which is attributed to the asymmetric stretching vibration of the W–O bonds in the WO_4^{2-} tetrahedral units. This peak position agrees well with previously reported FTIR data for scheelite-type $SrWO_4$ [36,40] indicating that the internal tetrahedral geometry of the tungstate group could be intact in both the pure $SrWO_4$ and the composite material. Broad O–H stretching and bending modes observed at about 3400 cm^{-1} and 1630 cm^{-1}, respectively, which are attributed to the adsorbed water on the particle surfaces, a common feature in oxide nanomaterials. Importantly, no additional absorption bands associated with impurity phases such as Fe_2O_3, FeOOH, or WO_3 are detected, indicating that the synthesized materials are phase-pure. The combination of ferrite (A–O/B–O) and tungstate (W–O) vibrational modes in the composite further supports the successful integration of both structures without chemical degradation.

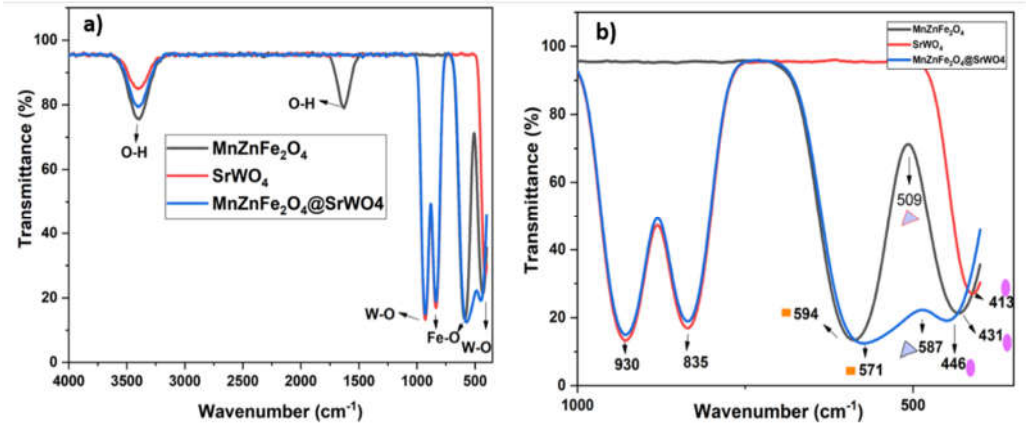

Figure 4. FTIR spectra of $MnZnFe_2O_4$, $SrWO_4$, and $MnZnFe_2O_4$@$SrWO_4$ shown in (a) full range and (b) the 1000–400 cm^{-1} region.

3.4. SEM and EDX Analysis

The morphology and particle size distribution of the synthesized materials were investigated using scanning electron microscopy (SEM), revealing distinct characteristics for each of the three samples including $MnZnFe_2O_4$, $SrWO_4$, and $MnZnFe_2O_4$@$SrWO_4$. The SEM image of $MnZnFe_2O_4$ (Figure 5a) shows that the particles form agglomerated clusters of nearly spherical nanoparticles. The particle size distribution for $MnZnFe_2O_4$, as indicated in the corresponding graph (Figure 5d), ranges from 25 nm to 40 nm, with the majority of particles falling between 30 nm and 35 nm. This narrow distribution suggests that the synthesis method was effective in producing relatively uniform particles. However, the presence of agglomeration, as seen in the SEM images, suggests that the nanoparticles tend to stick together due to strong magnetic dipole–dipole interactions. Such observations are consistent with previous studies on Mn-based ferrites, where a similar spherical morphology and moderate agglomeration were reported for $MnFe_2O_4$ synthesized by co-precipitation and solvothermal methods [41]. Such clustering has been well documented in Mn–Zn ferrites due to their high saturation magnetization and surface energy [42]. Though agglomerated, the individual particle boundaries remain visible, suggesting that primary crystallite growth was not significantly hindered during synthesis. The pure $SrWO_4$ sample (Figure 5b) displays a distinct faceted morphology, with grain sizes in the range of 35 nm to 60 nm and an average size of 50 nm (Figure 5e). These polyhedral features are typical of scheelite-type tungstates, which tend to crystallize with smooth edges due to the anisotropic growth rates of WO_4^{2-} tetrahedral units [36]. The relatively uniform grain boundaries and well-defined edges indicate good crystallinity, consistent with the strong diffraction peaks observed in XRD. The nucleation density in $SrWO_4$ appears higher than in the ferrite, which explain the slightly broader size distribution compared to $MnZnFe_2O_4$ [43]. In the composite $MnZnFe_2O_4$@$SrWO_4$ (Figure 5c), a noticeable shift in morphology is observed. It shows a significant reduction in particle size. The particle size distribution for the composite (Figure 5f) is much narrower, ranging from 5 nm to 30 nm, with the highest frequency of particles appearing

 doi:10.20944/preprints202601.1084.v1

in the 15 nm to 20 nm. This smaller size and more uniform distribution suggest that the $SrWO_4$ shell plays a key role in controlling the particle size of the $MnZnFe_2O_4$ heterostructure [44]. This reduction in particle size suggests that $SrWO_4$ plays a regulatory role during composite formation, limiting ferrite grain growth and promoting a higher nucleation rate. The finer morphology likely arises because WO_4^{2-} units adsorb onto ferrite nuclei, suppressing their coalescence and restricting further grain enlargement. Similar grain-refining effects have been reported in ferrite–oxide hybrid systems where tungstate and molybdate phases alter the growth kinetics. The reduced particle size in the composite indicates that the interface between $MnZnFe_2O_4$ and $SrWO_4$ is not merely physical but involves surface-level interactions that influence nucleation behavior [33]. The particle size decreases from 28 nm for $MnZnFe_2O_4$ and 49 nm for $SrWO_4$ to 26 nm for $MnZnFe_2O_4$@$SrWO_4$, which supports this interpretation. The reduction of particle size can enhance surface area, which can provide abundant active sites, leading to enhancement in performance for OER [45].

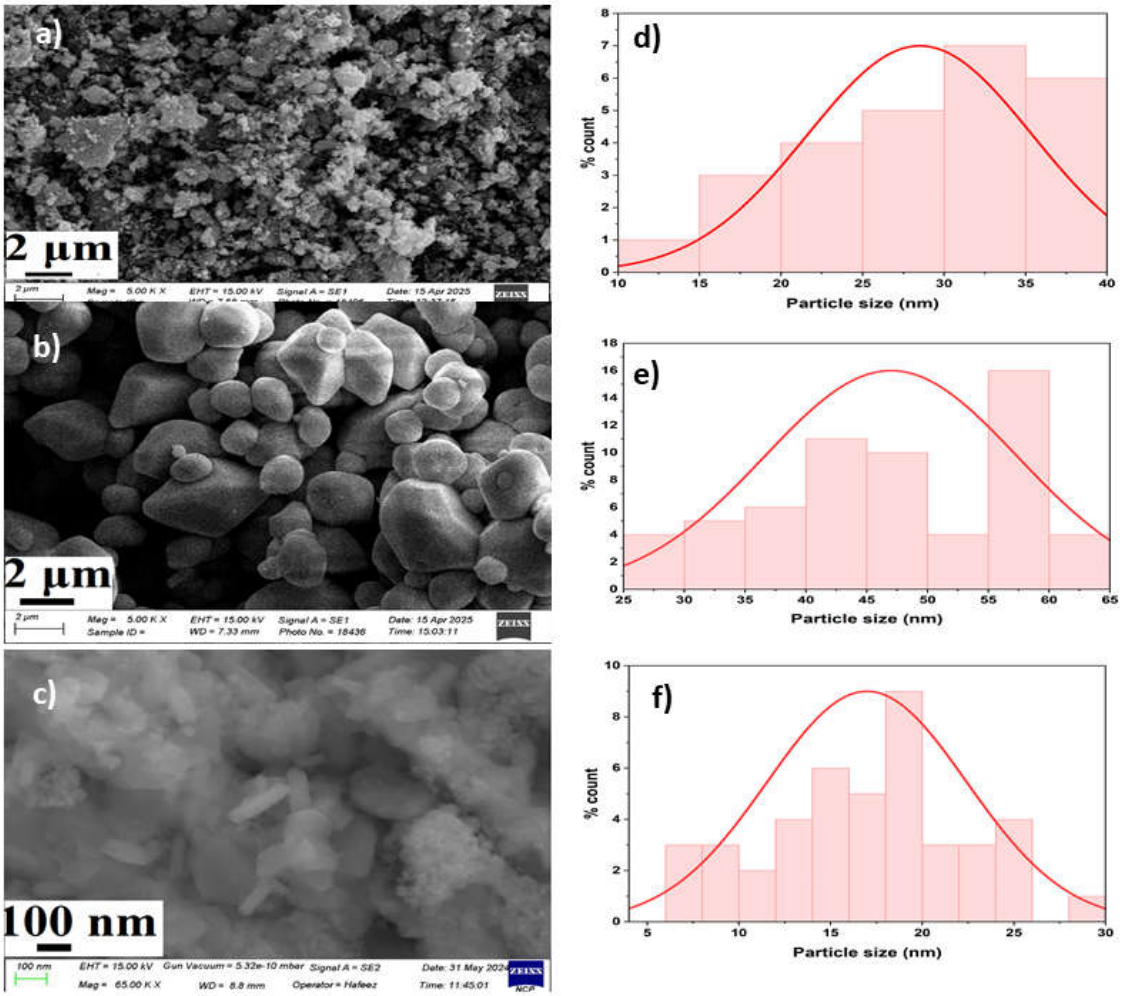

Figure 5. SEM images of a) $MnZnFe_2O_4$ b) $SrWO_4$ and c) $MnZnFe_2O_4$@$SrWO_4$, and particle size distribution of d) $MnZnFe_2O_4$ e) $SrWO_4$ and f) $MnZnFe_2O_4$@$SrWO_4$.

The EDX spectra of the synthesized materials are shown in Figure 6 confirming the presence of all expected elements. For $MnZnFe_2O_4$, distinct peaks of Mn, Zn, Fe, and O verify the formation of the spinel ferrite without detectable impurity phases. A small carbon signal appears due to residual surfactant from the low-temperature CTAB-assisted synthesis, which is commonly reported and does not affect phase purity. The $SrWO_4$ sample shows strong Sr, W, and O peaks with a nearly ideal Sr:W ratio, indicating successful formation of the scheelite phase. In the $MnZnFe_2O_4$@$SrWO_4$ composite, the simultaneous presence of Mn, Zn, Fe, Sr, W, and O confirms the coexistence of both $MnZnFe_2O_4$

 doi:10.20944/preprints202601.1084.v1

and $SrWO_4$ phases. No extra elemental peaks were observed, demonstrating that the composite is chemically pure and that the synthesis process did not introduce any unwanted species.

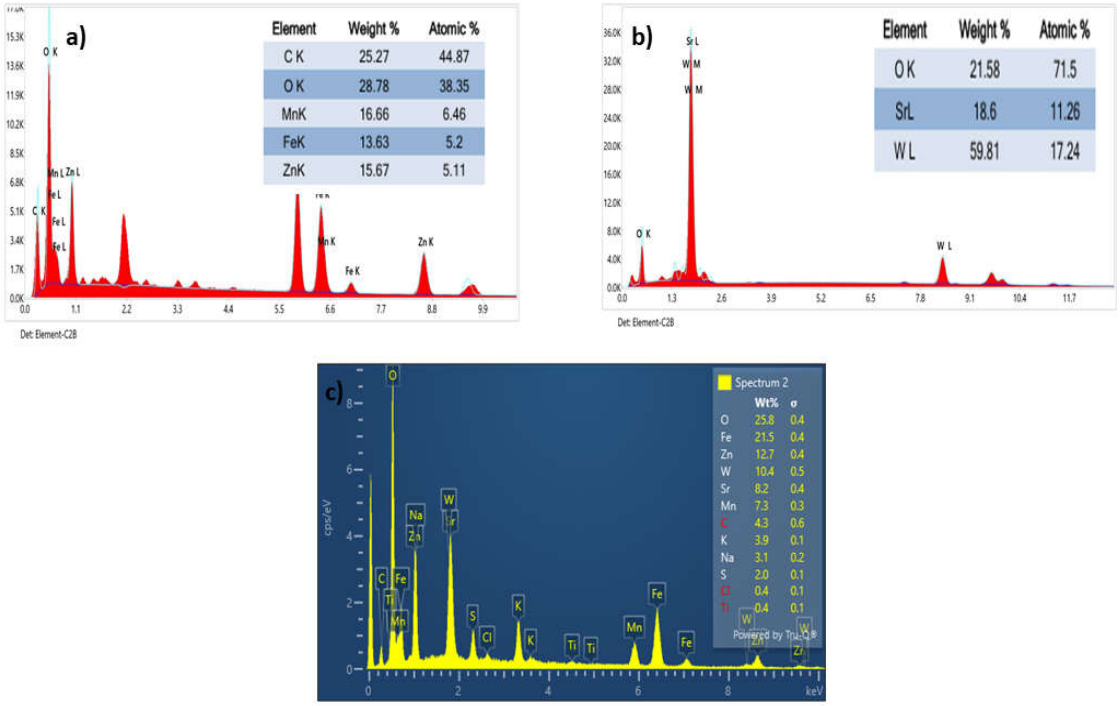

Figure 6. EDX spectra of a) $MnZnFe_2O_4$ b) $SrWO_4$ and c) $MnZnFe_2O_4$@$SrWO_4$.

3.5. Electrochemical OER Activity

The electrocatalytic OER behavior of $MnZnFe_2O_4$, $SrWO_4$, and $MnZnFe_2O_4$@$SrWO_4$ were evaluated in a standard three-electrode configuration using 1 M KOH, and the corresponding LSV curves, Tafel slopes, Nyquist plots and chronoamperometry results are shown in Figure 7 (a–e). All potentials are reported versus the reversible hydrogen electrode (RHE). All three materials show very small faradaic currents in the low potential region, followed by a rapid increase once the OER region is reached as shown in Figure 7a [23].

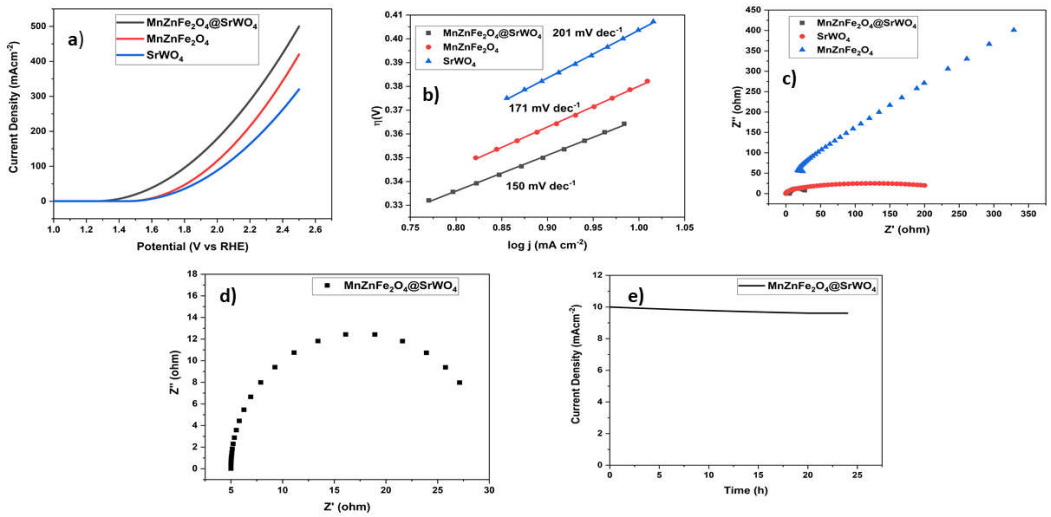

Figure 7. a) LSV curves of $MnZnFe_2O_4$, $SrWO_4$ and $MnZnFe_2O_4$@$SrWO_4$. b) Tafel plots of $MnZnFe_2O_4$, $SrWO_4$ and $MnZnFe_2O_4$@$SrWO_4$ in 1 M KOH. c) Nyquist plots of $MnZnFe_2O_4$, $SrWO_4$ and $MnZnFe_2O_4$@$SrWO_4$ in 1 M

 doi:10.20944/preprints202601.1084.v1

KOH. d) Nyquist plot of $MnZnFe_2O_4$@$SrWO_4$ in 1 M KOH. e) Stability test of $MnZnFe_2O_4$@$SrWO_4$ through chronoamperometric measurement at a constant applied η of 200 mV for 24 h in 1 M KOH.

3.5.1. LSV Study

A clear activity order $MnZnFe_2O_4$@$SrWO_4$ > $MnZnFe_2O_4$ > $SrWO_4$ is observed from LSV as shown in Figure 7 (a). The onset potential for oxygen evolution, defined as the potential at which the current density reaches ~1 mA cm^{-2}, is 1.40 V vs RHE for the $MnZnFe_2O_4$@$SrWO_4$ composite. In comparison, the onset potentials shift to more positive values of 1.52 V vs RHE for $MnZnFe_2O_4$ and 1.60 V vs RHE for $SrWO_4$. At a benchmark current density of 10 mA cm^{-2}, the $MnZnFe_2O_4$@$SrWO_4$ electrode requires an overpotential of only ~200 mV, markedly lower than those of pristine $MnZnFe_2O_4$ (380 mV) and $SrWO_4$ (400 mV). This means the composite needs ~180 to 200 mV less driving force than either individual oxide to sustain the same OER rate, indicating that the $MnZnFe_2O_4$/$SrWO_4$ interface creates genuinely more active and kinetically favorable sites rather than giving a simple additive effect. These values are better than or well comparable with the ferrite based electrocatalysts for OER reported in literature [5,6,17,46] as shown in Table 1, where the present OER activity of ~200 mV at 10 mA cm^{-2} for $MnZnFe_2O_4$@$SrWO_4$ is better than that of 247 mV for $MnFe_2O_4$/PANI [47], 273 mV for $CoFe_2O_4$/Ni foam [48], 230 mV for Fe-doped amorphous $NiWO_4$ [49], 235 mV for amorphous Ni–Fe tungstate ($NiFeWO_4$-3) [50], 310 mV for $NiCo_2O_4$@$NiWO_4$ (nanorods arrays) [51], 244 mV of Ni_2Fe_1–O [52], 260 mV of $Na_{0.08}Ni_{0.9}Fe_{0.1}O_2$ [53], 267 mV of S–$NiFe_2O_4$ [54], and 262 mV of $NiFe_2O_4$ quantum dot [55]. In short, these comparisons show that heterostructure ($MnZnFe_2O_4$@$SrWO_4$) not only outperforms its own single component counterparts but also matches and surpass many advanced ferrite and tungstate based OER, placing $MnZnFe_2O_4$@$SrWO_4$ firmly in the high-performance regime.

Beyond onset, the current density on the composite electrode increases much more steeply with potential than on the single-component catalysts. At a given anodic part in the OER region (e.g. around 1.4–1.8 V vs RHE), the $MnZnFe_2O_4$@$SrWO_4$ electrode delivers noticeably higher current densities than $MnZnFe_2O_4$, while $SrWO_4$ shows the lowest response. This behavior clearly demonstrates that the coupling of the spinel ferrite and scheelite tungstate phases in the composite generates a larger number of electrochemically active sites and more favorable charge-transfer characteristics, which together account for the superior LSV performance of $MnZnFe_2O_4$@$SrWO_4$ toward the oxygen evolution reaction.

Table 1. Comparison of OER performance of $MnZnFe_2O_4$, $SrWO_4$, and $MnZnFe_2O_4$@$SrWO_4$ with the reported oxide based electrocatalysts for OER.

Catalyst	Electrolyte	η_{10} (mV)	References
$MnFe_2O_4$/PANI	1 M KOH	247	[47]
$CoFe_2O_4$/Ni foam	1 M KOH	273	[48]
Fe-doped amorphous $NiWO_4$	1 M KOH	230	[49]
Amorphous Ni–Fe tungstate ($NiFeWO_4$-3)	1 M KOH	235	[50]
$NiCo_2O_4$@$NiWO_4$ (nanorods arrays)	1 M KOH	310	[51]
Ni_2Fe_1–O	1 M KOH	244	[52]
$Na_{0.08}Ni_{0.9}Fe_{0.1}O_2$	1 M KOH	260	[53]
S–$NiFe_2O_4$	1 M KOH	267	[54]
$NiFe_2O_4$ quantum dot	1 M KOH	262	[55]
$SrWO_4$	1 M KOH	400	This work
$MnZnFe_2O_4$	1 M KOH	380	This work
$MnZnFe_2O_4$@$SrWO_4$	1 M KOH	200	This work

 doi:10.20944/preprints202601.1084.v1

3.5.2. Tafel Slope and Kinetics

To gain quantitative insight into the reaction kinetics, Tafel plots in Figure 7(b) were constructed from the LSV data according to the Tafel relationship in equation 4.

$$\eta = a + b\log(j) \quad (4)$$

where η is the overpotential, a is the intercept, j is the current density and b is the Tafel slope. The resulting plots are shown in Figure 7(b). The extracted Tafel slopes are approximately 150 mV dec^{-1} for $MnZnFe_2O_4$@$SrWO_4$, 171 mV dec^{-1} for $MnZnFe_2O_4$ and 201 mV dec^{-1} for $SrWO_4$. The heterostructure $MnZnFe_2O_4$@$SrWO_4$ exhibits the smaller Tafel slope, suggesting its faster reaction kinetics for OER, thereby a smaller increment in overpotential is required to achieve a given increase in current density. This behavior indicates that the apparent OER kinetics are most favorable on the composite electrode, whereas the larger slopes of pristine $MnZnFe_2O_4$ and $SrWO_4$ reflect more pronounced polarization losses and slower charge transfer processes. Although the absolute values (150 to 200 mV dec^{-1}) are higher than the "ideal" 40 to 60 mV dec^{-1} typically observed for highly conductive NiFe-based nanostructures and layered double hydroxides [56] they are fully comparable to many spinel ferrite and tungstate systems. For example, $CoFe_2O_4$@MWCNT and $Fe_2(WO_4)_3$/rGO electrodes show OER Tafel slopes of ~166 and ~130 mV dec^{-1}, respectively [57] while Nd-doped $BaWO_4$ nanospindles exhibit a slope of ~158 mV dec^{-1} [58]. Thus, the $MnZnFe_2O_4$@$SrWO_4$ heterostructure catalyst performs at least as well as, and in several cases better than, other ferrite/tungstate-based OER electrocatalysts reported in the literature.

From a mechanistic point of view, Tafel slopes in the range of 150 to 200 mV dec^{-1} are best regarded as apparent kinetic parameters rather than direct fingerprints of a single rate-determining step. In practical OER electrodes, the ideal values (≈40 to 120 mV dec^{-1}) are often inflated by uncompensated resistance, finite electronic conductivity, surface-coverage effects and early mass-transport or bubble limitations, which are all relevant for semiconducting ferrite and tungstate-based oxides. In this context, the absolute values of 201 mV dec^{-1} ($SrWO_4$), 171 mV dec^{-1} ($MnZnFe_2O_4$) and 150 mV dec^{-1} ($MnZnFe_2O_4$@$SrWO_4$) are most reasonably interpreted as a convolution of charge-transfer and transport or ohmic effects [59]. The important result is the systematic decrease in slope from $SrWO_4$ to $MnZnFe_2O_4$ to the heterostructure $MnZnFe_2O_4$@$SrWO_4$, which tracks the trend in overpotential and current density and shows that the $MnZnFe_2O_4$@$SrWO_4$ architecture effectively eases kinetic limitations and enhances the overall OER performance. The Tafel slope of 150, 171, and 201 mV dec^{-1} of $MnZnFe_2O_4$@$SrWO_4$, $MnZnFe_2O_4$, and $SrWO_4$ catalysts, respectively, suggests that the first electron transfer is the rating determining step (Catalyst* (active site) + OH^- → Catalyst*OH + e^-) [6,17,46]. However, for $MnZnFe_2O_4$@$SrWO_4$ catalyst, the shift from 201 to 150 mV dec^{-1} confirms that the heterostructure has successfully lowered the barrier for the first electron transfer, and enhanced the reaction kinetics for OER.

3.5.3. Electrochemical Impedance Spectroscopy (EIS) Study

Electrochemical impedance spectroscopy was carried out to examine the interfacial charge transfer behavior of the three electrodes. The Nyquist plots in Fig 7 (c) show depressed semicircles in the high–medium frequency region, which can be described by a Randles-type circuit in which the semicircle diameter corresponds to the charge-transfer resistance (R_{ct}) at the electrode/electrolyte interface. Among the investigated samples, $MnZnFe_2O_4$@$SrWO_4$ displays the smallest semicircle (larger magnification is shown in Figure 7(d)), and $SrWO_4$ shows an intermediate arc, while $MnZnFe_2O_4$ exhibits the largest arc. This sequence clearly indicates that the heterostructure composite possesses the lowest R_{ct} and the most facile electron transfer during OER, whereas pristine $MnZnFe_2O_4$ suffers from pronounced interfacial resistance. This behavior is in line with previous reports on ferrite and tungstate-based catalysts, where coupling the active phase with a conductive or synergistic component markedly decreases R_{ct} and enhances electrocatalytic activity. For example, $MnFe_2O_4$/graphene aerogel and $MnFe_2O_4$/PANI composites show substantially smaller Nyquist semicircles and lower R_{ct} values than bare $MnFe_2O_4$, evidencing more efficient charge transfer at the modified interface [60]. Similarly, metal tungstate nanoparticles supported on reduced graphene

 doi:10.20944/preprints202601.1084.v1

oxide/silica templates exhibit reduced R_{ct} compared with unsupported $NiWO_4$, which is directly correlated with their improved OER performance [61].

3.5.4. Chronoamperometric Stability Study

The long-term stability of $MnZnFe_2O_4$@$SrWO_4$ catalyst for OER was evaluated through chronoamperometric measurement at a constant applied η of 200 mV for 24 h in 1 M KOH as shown in Figure 7(e). The composite retains >94% of its initial current density after 24 h of electrolysis, indicating its good durability. The absence of any sharp decay or fluctuation in the current profile indicates that the heterostructure film adheres well to the substrate and does not undergo significant dissolution, reconstruction or loss of active sites under continuous OER operation. This stable response confirms that the $MnZnFe_2O_4$@$SrWO_4$ architecture combines good catalytic activity with excellent electrochemical durability. This suggests that the $SrWO_4$ integration effectively stabilizes the ferrite surface, providing a robust architecture suitable for practical alkaline water electrolysis.

3.5.5. Cyclic Voltammetry Study

Cyclic voltammetry was carried out within a selected potential window where no obvious faradic processes occur in order to investigate the non-faradic capacitive behavior of the catalyst as shown in Figure 8(a-c). In this region the measured current mainly originates from electrochemical double layer charging. As the scan rate was increased from 10 to 50 mV s^{-1}, a proportional increase in current response was observed for all samples, confirming that the chosen potential range is suitable for evaluating the double layer capacitance. The double-layer capacitance (C_{dl}) was determined from the dependence of the capacitive current on scan rate. The anodic and cathodic current densities at a fixed potential within the non-faradic region were used to calculate the capacitive current differences ($\Delta j = j_a - j_c$), and the plot of Δj versus scan rate (10 to 50 mV s^{-1}) exhibited good linearity. The slope divided by 2 of these plots was taken as C_{dl} values. Using this approach, the C_{dl} values (Figure 8(d-f)) of 9.35 mF cm^{-2} for $MnZnFe_2O_4$@$SrWO_4$, 3.96 mF cm^{-2} for $MnZnFe_2O_4$ and 2.55 mF cm^{-2} for $SrWO_4$ were obtained indicating a prominent capacitive response for the heterostructured catalyst toward OER activity. Using this approach, the C_{dl} values of 9.35 mF cm^{-2} for $MnZnFe_2O_4$@$SrWO_4$, 3.96 mF cm^{-2} for $MnZnFe_2O_4$ and 2.55 mF cm^{-2} for $SrWO_4$ were obtained indicating a prominent capacitive response for the heterostructured catalyst toward OER activity. The C_{dl} values of 9.35 mF cm^{-2} for $MnZnFe_2O_4$@$SrWO_4$, is higher than that of 3.96 mF cm^{-2} for $MnZnFe_2O_4$ and 2.55 mF cm^{-2} for $SrWO_4$, which suggests that the $MnZnFe_2O_4$@$SrWO_4$, exhibits higher electrochemically active surface area than that of $MnZnFe_2O_4$ and $SrWO_4$. This further suggests that the $MnZnFe_2O_4$@$SrWO_4$ catalyst exhibits abundant active sites than that of $MnZnFe_2O_4$ and $SrWO_4$, leading to the high performance of $MnZnFe_2O_4$@$SrWO_4$ for OER.

 doi:10.20944/preprints202601.1084.v1

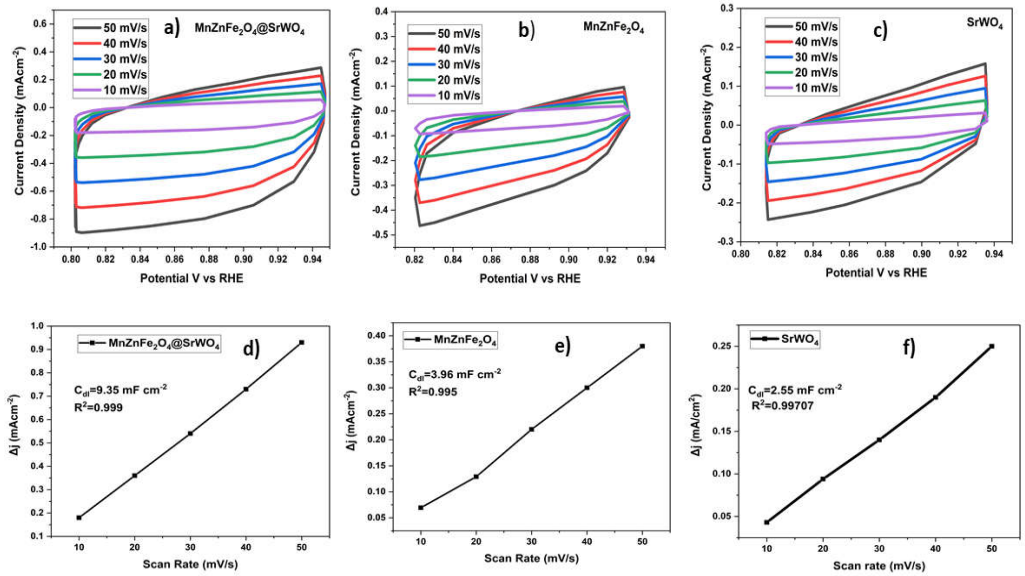

Figure 8. Cyclic voltammetry curves of a) $MnZnFe_2O_4$@$SrWO_4$, b) $MnZnFe_2O_4$, and c) $SrWO_4$ at various scan rate in 1 M KOH. The difference in anodic and cathodic current densities as a function of the scan rate to evaluate the double-layer capacitances of d) $MnZnFe_2O_4$@$SrWO_4$, e) $MnZnFe_2O_4$, and f) $SrWO_4$.

4. Conclusion

In this work, we prepared a $MnZnFe_2O_4$@$SrWO_4$ heterostructure and evaluated it as an OER electrocatalyst in 1.0 M KOH. XRD, FTIR and UV–Vis analyses confirmed the coexistence of spinel ferrite and scheelite-type tungstate phases, while SEM–EDX showed a more compact and uniformly distributed morphology compared with the individual oxides. Electrochemical studies revealed that $MnZnFe_2O_4$@$SrWO_4$ requires a lower overpotential to reach 10 mA cm^{-2}, with a smaller Tafel slope and lesser charge-transfer resistance when compared to that of pristine $MnZnFe_2O_4$ and $SrWO_4$. Chronoamperometric tests further indicated stable performance over prolonged operation, confirming good durability under alkaline OER conditions. The enhanced activity is attributed to the synergistic interaction at the ferrite–tungstate interface, which promotes charge transfer and improves the utilization of active sites. These results indicate that $MnZnFe_2O_4$@$SrWO_4$ and related ferrite–tungstate composites are promising low-cost candidates for OER in alkaline water electrolysis.

Author Contributions: I.J. and F.N. developed the idea, started the project, and contributed to the synthesis, characterization, and performance of electrocatalysts for OER. I.J., F.N., H.Y.H., and M.I.J. supervised and directed the project. I. J. wrote the original draft. I.J., F.N., M.R., V.G., H.Y.H., and M.I.J., contributed to the revision of the manuscript. The manuscript is finalized by discussion with all authors.

Declaration of Competing Interest: The authors declare that they have no known competing financial interests or personal relationships that could have appeared to influence the work reported in this paper.

Funding: This research did not receive any specific grant from funding agencies in the public, commercial, or not-for-profit sectors.

Acknowledgments: I.J., F.N., and M.R. sincerely express their heartfelt gratitude to the University of Wah for providing all the available facilities. M.I.J and H.Y.H acknowledge financial support from the Research Grants Council of Hong Kong (grant no. CityU 21203518 and F-CityU106/18), Innovation and Technology Commission (grant no. MHP/104/21), Shenzhen Science Technology and Innovation Commission (grant no. JCYJ20210324125612035, JCYJ20250604190210013, R-IND12303 and R-IND12304), City University of Hong Kong (grant no. 7020113, 9229160, 9360140, 7005289, 7005580, 7005720, 9667213, 9667229, 9680331 and 9678291), NJU National Fellowship Initiative (NJU NFI), and 2025 UAiTED Faculty Exchange Scholarship.

 doi:10.20944/preprints202601.1084.v1

Data Availability: All data generated or analyzed during this study are included in this published article and its Supplementary Information files. Further data is available from the corresponding author on reasonable request.

References

1. M.-I. Jamesh, H. Tong, M. Du, W. Niu, G. Jia, K.-C. Cheng, C.-W. Hsieh, H.-H. Shen, B. Xu, Y. Tian, X. Xu, H.-Y. Hsu, Advancement of technology towards developing perovskite-based solar cells for renewable energy harvesting and energy transformation applications, npj Materials Sustainability, 3 (2025) 29.
2. B. Dong, M. Wei, Y. Li, Y. Yang, W. Ma, Y. Zhang, Y. Ran, M. Cui, Z. Su, Q. Fan, Z. Bi, T. Edvinsson, Z. Ding, H. Ju, S. You, S.M. Zakeeruddin, X. Li, A. Hagfeldt, M. Grätzel, Y. Liu, Self-assembled bilayer for perovskite solar cells with improved tolerance against thermal stresses, Nature Energy, 10 (2025) 342-353.
3. S. Li, Y. Xiao, R. Su, W. Xu, D. Luo, P. Huang, L. Dai, P. Chen, P. Caprioglio, K.A. Elmestekawy, M. Dubajic, C. Chosy, J. Hu, I. Habib, A. Dasgupta, D. Guo, Y. Boeije, S.J. Zelewski, Z. Lu, T. Huang, Q. Li, J. Wang, H. Yan, H.-H. Chen, C. Li, B.A.I. Lewis, D. Wang, J. Wu, L. Zhao, B. Han, J. Wang, L.M. Herz, J.R. Durrant, K.S. Novoselov, Z.-H. Lu, Q. Gong, S.D. Stranks, H.J. Snaith, R. Zhu, Coherent growth of high-Miller-index facets enhances perovskite solar cells, Nature, 635 (2024) 874-881.
4. Y. Yang, H. Chen, C. Liu, J. Xu, C. Huang, C.D. Malliakas, H. Wan, A.S.R. Bati, Z. Wang, R.P. Reynolds, I.W. Gilley, S. Kitade, T.E. Wiggins, S. Zeiske, S. Suragtkhuu, M. Batmunkh, L.X. Chen, B. Chen, M.G. Kanatzidis, E.H. Sargent, Amidination of ligands for chemical and field-effect passivation stabilizes perovskite solar cells, Science, 386 (2024) 898-902.
5. M.-I. Jamesh, H. Tong, S.P. Santoso, W. Niu, J.-J. Kai, C.-W. Hsieh, K.-C. Cheng, F.-F. Li, B. Han, J.C. Colmenares, H.-Y. Hsu, Recent advances in developing nanoscale electro-/photocatalysts for hydrogen production: modification strategies, charge-carrier characterizations, and applications, Nanoscale, 16 (2024) 18213-18250.
6. M.-I. Jamesh, D. Hu, J. Wang, F. Naz, J. Feng, L. Yu, Z. Cai, J.C. Colmenares, D.-J. Lee, P.K. Chu, H.-Y. Hsu, Recent advances in noble metal-free electrocatalysts to achieve efficient alkaline water splitting, Journal of Materials Chemistry A, (2024) 11771-11820.
7. M.-I. Jamesh, A. Akila, D. Sudha, K. Gnana Priya, V. Sivaprakash, A. Revathi, Fabrication of Earth-Abundant Electrocatalysts Based on Green-Chemistry Approaches to Achieve Efficient Alkaline Water Splitting—A Review, Sustainability, 14 (2022) 16359.
8. J. Wang, M.-I. Jamesh, Q. Gao, B. Han, R. Sun, H.-Y. Hsu, C. Zhou, Z. Cai, Semimetallic hydroxide materials for electrochemical water oxidation, Science China Materials, (2024) 10.1007/s40843-40023-42802-40848.
9. M.-I. Jamesh, Improved In Vitro and In Vivo Corrosion Resistance of Mg and Mg Alloys by Plasma Ion Implantation and Deposition Techniques—A Mini-Review, Lubricants, 10 (2022) 255.
10. M.I. Jamesh, R. Boxman, N.J. Nosworthy, I. Falconer, P.K. Chu, M.M. Bilek, A. Kondyurin, R. Ganesan, D.R. McKenzie, Graded metal carbon protein binding films prepared by hybrid cathodic arc—Glow discharge plasma assisted chemical vapor deposition, Surface and Coatings Technology, 265 (2015) 222-234.
11. L. Shi, M.P. Bucknall, T.L. Young, M. Zhang, L. Hu, J. Bing, D.S. Lee, J. Kim, T. Wu, N. Takamure, D.R. McKenzie, S. Huang, M.A. Green, A.W.Y. Ho-Baillie, Gas chromatography–mass spectrometry analyses of encapsulated stable perovskite solar cells, Science, 368 (2020) eaba2412.
12. Y. Tang, C.H. Mak, J. Zhang, G. Jia, K.-C. Cheng, H. Song, M. Yuan, S. Zhao, J.-J. Kai, J.C. Colmenares, H.-Y. Hsu, Unravelling the Interfacial Dynamics of Bandgap Funneling in Bismuth-Based Halide Perovskites, Advanced Materials, 35 (2023) 2207835.
13. Y. Tang, C.H. Mak, R. Liu, Z. Wang, L. Ji, H. Song, C. Tan, F. Barrière, H.-Y. Hsu, In Situ Formation of Bismuth-Based Perovskite Heterostructures for High-Performance Cocatalyst-Free Photocatalytic Hydrogen Evolution, Advanced Functional Materials, 30 (2020) 2006919.
14. E. Ugur, A.A. Said, P. Dally, S. Zhang, C.E. Petoukhoff, D. Rosas-Villalva, S. Zhumagali, B.K. Yildirim, A. Razzaq, S. Sarwade, A. Yazmaciyan, D. Baran, F. Laquai, C. Deger, I. Yavuz, T.G. Allen, E. Aydin, S. De Wolf, Enhanced cation interaction in perovskites for efficient tandem solar cells with silicon, Science, 385 (2024) 533-538.

 doi:10.20944/preprints202601.1084.v1

15. S. Liu, J. Li, W. Xiao, R. Chen, Z. Sun, Y. Zhang, X. Lei, S. Hu, M. Kober-Czerny, J. Wang, F. Ren, Q. Zhou, H. Raza, Y. Gao, Y. Ji, S. Li, H. Li, L. Qiu, W. Huang, Y. Zhao, B. Xu, Z. Liu, H.J. Snaith, N.G. Park, W. Chen, Buried interface molecular hybrid for inverted perovskite solar cells, Nature, 632 (2024) 536-542.
16. H. Tang, Z. Shen, Y. Shen, G. Yan, Y. Wang, Q. Han, L. Han, Reinforcing self-assembly of hole transport molecules for stable inverted perovskite solar cells, Science, 383 (2024) 1236-1240.
17. M.I. Jamesh, M. Harb, Tuning the electronic structure of the earth-abundant electrocatalysts for oxygen evolution reaction (OER) to achieve efficient alkaline water splitting – A review, Journal of Energy Chemistry, 56 (2021) 299-342.
18. M.I. Jamesh, Recent progress on earth abundant hydrogen evolution reaction and oxygen evolution reaction bifunctional electrocatalyst for overall water splitting in alkaline media, Journal of Power Sources, 333 (2016) 213-236.
19. M.-I. Jamesh, M. Harb, Recent advances on hydrogen production through seawater electrolysis, Materials Science for Energy Technologies, 3 (2020) 780-807.
20. H. Araújo, B. Šljukić, S. Gago, D.M. Santos, The current state of transition metal-based electrocatalysts (oxides, alloys, POMs, and MOFs) for oxygen reduction, oxygen evolution, and hydrogen evolution reactions, Frontiers in Energy Research, 12 (2024) 1373522.
21. X. Wu, F. Meharban, J. Xu, Z. Zhao, X. Tang, L. Tan, Y. Song, W. Hu, Q. Xiao, C. Lin, Anode Alchemy on Multiscale: Engineering from Intrinsic Activity to Impedance Optimization for Efficient Water Electrolysis, Small, 21 (2025) 2411704.
22. U. Farooq, T. Ahmad, F. Naaz, S.u. Islam, Review on metals and metal oxides in sustainable energy production: progress and perspectives, Energy & Fuels, 37 (2023) 1577-1632.
23. Y. Zhang, K. Nie, L. Yi, B. Li, Y. Yuan, Z. Liu, W. Huang, Recent Advances in Engineering of 2D Materials--Based Heterostructures for Electrochemical Energy Conversion, Advanced Science, 10 (2023) 2302301.
24. I. Fareed, M.D. Khan, S. Murtaza, Z.U. Rehman, M.U. Farooq, F.K. Butt, M. Tahir, Investigating metal (M= Mn, Fe, and Ni)-doped Co (OH) 2 nanofibers for electrocatalytic oxygen evolution and electrochemical biosensing performance, RSC advances, 14 (2024) 26556-26567.
25. A.B. Ibrahim, M.A. Habib, S. Munir, F. Ahmad, M.I. Khan, A. Shanableh, Enhanced electrocatalytic activity of NiWPd nanocrystals for oxygen reduction reaction in fuel cells, Journal of Organometallic Chemistry, (2025) 123796.
26. Y. Mao, X. Wang, J. Wu, Y. Min, Q. Li, Q. Xu, Enhance the performance of OER electrocatalyst via synergistic oxygen vacancies and NiFe2O4-phosphorene heterostructure, Journal of Alloys and Compounds, 997 (2024) 174949.
27. S. Jabeen, M. Saleem, F. Mumtaz, S. Javed, M. Ali, M.Z. Khan, J.-H. Koh, A. Maqbool, A.H. Baluch, M.B.K. Niazi, Coupling the power of spinel nanoparticles: dual-function metal ferrite catalysts for advanced piezo-photocatalytic and electrocatalytic water splitting, Journal of Materials Chemistry A, (2025).
28. L. Zhou, C. Wu, D. Guo, Y. Zhu, C. Wang, X.a. Chen, S. Wang, Highly efficient catalytic conversion of polysulfides: iron-based oxides, Catalysis Science & Technology, 14 (2024) 5161-5175.
29. V. Jeyavani, S. Manoj, S.P. Mukherjee, Effect of Transition Metals (Mn, Co, Ni, and Zn) in Size-Controlled Metal Ferrite Nanocrystals on the Electrocatalytic Oxygen Evolution Reaction, ACS Applied Nano Materials, 7 (2024) 17776-17785.
30. B. Ning, S. He, X. Lin, F.-X. Xiao, Interface engineering: enhanced catalysis through precise control of metal nanocluster transformation, Inorganic Chemistry, 63 (2024) 23742-23748.
31. X. Wu, Q. Yan, H. Wang, D. Wu, H. Zhou, H. Li, S. Yang, T. Ma, H. Zhang, Heterostructured catalytic materials as advanced electrocatalysts: classification, synthesis, characterization, and application, Advanced Functional Materials, 34 (2024) 2404535.
32. W. Zhao, Z. Wei, C. Li, M. Ding, Composite ZnFe2O4/SrWO4 hollow microspheres as catalyst for high-performance photo-Fenton degradation, Ceramics International, 50 (2024) 24063-24069.
33. S.D. Waghmare, S.P. Phulwale, S.m.F. Shaikh, A.M. Gaikwad, A.S. Thosar, R.G. Bobade, R.C. Ambare, P.N. Thonge, S.D. Dhas, Tungsten-doped bismuth ferrite nanoparticle electrodes for energy storage application, Journal of Materials Science: Materials in Electronics, 36 (2025) 1859.

 doi:10.20944/preprints202601.1084.v1

34. A. Shebl, A. Hassan, D.M. Salama, M.E. Abd El-Aziz, M.S. Abd Elwahed, Template-free microwave-assisted hydrothermal synthesis of manganese zinc ferrite as a nanofertilizer for squash plant (Cucurbita pepo L), Heliyon, 6 (2020).
35. J.-H. Wi, J.-Y. Jung, S.-G. Park, Synthesis of rare-earth-doped strontium tungstate phosphor at room temperature and applied flexible composite, Materials, 15 (2022) 8922.
36. C. Sridhar, N. Sahu, Y.-S. Seo, I. Rabani, G. Turpu, S. Tigga, G. Padmaja, Comparative Electrochemical, Photocatalytic, and Photoluminescence Studies in SrWO4 and rGO-SrWO4 Nanocomposites, Journal of Electronic Materials, 52 (2023) 3759-3773.
37. T.S. Fathima, S. Balamurugan, S. Ashika, Stabilizing the scheelite AWO4 (A= Ba, Sr, Ca) phase materials by combustion followed by heat treatment, Emergent Materials, 6 (2023) 1127-1134.
38. J. Chen, X. Yang, C. Jiang, Y. Wang, L. Zhou, M. Wu, Second-phase-induced fluorescence quenching in non-equivalent substituted red phosphors, RSC advances, 12 (2022) 29338-29345.
39. D. Lachowicz, A. Kmita, M. Gajewska, E. Trynkiewicz, M. Przybylski, S.E. Russek, K.F. Stupic, D.A. Woodrum, K.R. Gorny, Z.J. Celinski, Aqueous Dispersion of Manganese–Zinc Ferrite Nanoparticles Protected by PEG as a T2 MRI Temperature Contrast Agent, International journal of molecular sciences, 24 (2023) 16458.
40. S. Shanthi, N.A. Little Flower, R. Annie Sujatha, T. Sabari Girisun, K.M. Rahulan, Defect--Induced Non--Linear Optical Studies of Chromium--Doped Strontium Tungstate Nanostructures, ChemistrySelect, 9 (2024) e202401483.
41. W. Shatti, Z.M.A. Abbas, Z. Khodair, Co-precipitation method for the preparation of Mn-Zn Ferrite and study their Structural and Magnetic properties, JJ. Ovonic Res., 18 (2022) 473-479.
42. N. Abu-Elsaad, A. Nawara, Effect of Cu substitution on magnetic and photocatalytic properties of Mn–ZnFe2O4 nanoparticles, Journal of Materials Science, 59 (2024) 4167-4185.
43. M. Kowalkinska, P. Głuchowski, T. Swebocki, T. Ossowski, A. Ostrowski, W. Bednarski, J. Karczewski, A. Zielińska-Jurek, Scheelite-type wide-bandgap ABO4 compounds (A= Ca, Sr, and Ba; B= Mo and W) as potential photocatalysts for water treatment, The Journal of Physical Chemistry C, 125 (2021) 25497-25513.
44. Z. Dong, Z. Ma, L. Yu, Y. Liu, Achieving high strength and ductility in ODS-W alloy by employing oxide@ W core-shell nanopowder as precursor, Nature communications, 12 (2021) 5052.
45. M. Cai, S. Liu, J. Cai, L. Zhao, X. Wei, M. Guo, S. Lin, Microwave-assisted synthesis of mesoporous MgO@ carbon hybrid nanocomposites to enhance the catalytic degradation of paraoxon toxin, Journal of Environmental Chemical Engineering, 10 (2022) 107905.
46. J. Mohammed-Ibrahim, A review on NiFe-based electrocatalysts for efficient alkaline oxygen evolution reaction, Journal of Power Sources, 448 (2020) 227375.
47. I. Robina, B. Alotaibi, S. Ibrahim, H.A. Alyousef, A.W. Alrowaily, F.N. Almufleh, A.M. Alotaibi, Hydrothermal Synthesis of MnFe2O4-Embedded Polyaniline Nanocomposite for Enhancement in OER, Journal of the Indian Chemical Society, (2025) 101817.
48. S. Zhu, J. Lei, Y. Qin, L. Zhang, L. Lu, Spinel oxide CoFe 2 O 4 grown on Ni foam as an efficient electrocatalyst for oxygen evolution reaction, RSC advances, 9 (2019) 13269-13274.
49. H. N. Dhandapani, R. Madhu, A. De, M.A. Salem, B. Ramesh Babu, S. Kundu, Tuning the surface electronic structure of amorphous NiWO4 by doping Fe as an electrocatalyst for OER, Inorganic Chemistry, 62 (2023) 11817-11828.
50. H. Chen, X. Yang, Y. Wang, G. Zhang, N. Luan, Q. Zhang, F. He, S. Lv, X. Yu, X. Liu, Scale-up synthesis of amorphous Ni–Fe tungstate for highly-efficient oxygen evolution reaction, Chemical Communications, 61 (2025) 5970-5973.
51. X. Du, Q. Shao, X. Zhang, Metal tungstate dominated NiCo2O4@ NiWO4 nanorods arrays as an efficient electrocatalyst for water splitting, International Journal of Hydrogen Energy, 44 (2019) 2883-2888.
52. C. Dong, T. Kou, H. Gao, Z. Peng, Z. Zhang, Eutectic-Derived Mesoporous Ni-Fe-O Nanowire Network Catalyzing Oxygen Evolution and Overall Water Splitting, Advanced Energy Materials, (2017) 1701347.
53. B. Weng, F. Xu, C. Wang, W. Meng, C.R. Grice, Y. Yan, A layered Na1-xNiyFe1-yO2 double oxide oxygen evolution reaction electrocatalyst for highly efficient water-splitting, Energy & Environmental Science, 10 (2017) 121-128.

 doi:10.20944/preprints202601.1084.v1

54. J. Liu, D. Zhu, T. Ling, A. Vasileff, S.-Z. Qiao, S-NiFe2O4 ultra-small nanoparticle built nanosheets for efficient water splitting in alkaline and neutral pH, Nano Energy, 40 (2017) 264-273.
55. H. Yang, Y. Liu, S. Luo, Z. Zhao, X. Wang, Y. Luo, Z. Wang, J. Jin, J. Ma, Lateral-Size-Mediated Efficient Oxygen Evolution Reaction: Insights into the Atomically Thin Quantum Dot Structure of NiFe2O4, ACS Catalysis, 7 (2017) 5557-5567.
56. Y. Yao, J. Lyu, X. Li, C. Chen, F. Verpoort, J. Wang, Z. Pan, Z. Kou, A review of efficient electrocatalysts for the oxygen evolution reaction at large current density, DeCarbon, 5 (2024) 100062.
57. M. Afaq, M. Shahid, I. Ahmad, S. Yousaf, A. Alazmi, M. Mahmoud, I.H. El Azab, M.F. Warsi, Large-scale sonochemical fabrication of a Co 3 O 4–CoFe 2 O 4@ MWCNT bifunctional electrocatalyst for enhanced OER/HER performances, RSC advances, 13 (2023) 19046-19057.
58. S. Swathi, M. Priyanga, Y. Rathinam, R. Ganesan, A.G. Al-Sehemi, D. Velauthapillai, Neodymium-doped novel barium tungstate nanospindles for the enhanced oxygen evolution reaction, ACS omega, 8 (2023) 3745-3754.
59. T. Shinagawa, A.T. Garcia-Esparza, K. Takanabe, Insight on Tafel slopes from a microkinetic analysis of aqueous electrocatalysis for energy conversion, Scientific reports, 5 (2015) 13801.
60. K.S. Bejigo, B.J. Park, J.H. Kim, H.H. Yoon, Synthesis and Evaluation of Graphene Aerogel--Supported MnxFe3− xO4 for Oxygen Reduction in Urea/O2 Fuel Cells, ChemistryOpen, 8 (2019) 615-620.
61. R. Amin, A.E. Fetohi, D. Khater, J. Lin, Y. Wang, C. Wang, K. El-Khatib, Selenium-transition metal supported on a mixture of reduced graphene oxide and silica template for water splitting, RSC advances, 13 (2023) 15856-15871.